

36. Barkey, D. P., Watt, D., Liu, Z. & Raber, S. The role of induced convection in branched electrodeposition morphology selection. *J. Electrochem. Soc.* 141, 1206–1212 (1994).
37. Livermore, C. & Wong, P. Z. Convection and turbulence effects in strongly driven electrochemical deposition. *Phys. Rev. Lett.* 72, 3847–3850 (1994).
38. Heur, V., Chazalviel, J. N. & Rosso, M. Coupling of drift, diffusion, and electroconvection, in the vicinity of growing electrodeposits. *Phys. Rev. E* 48, 1279–1295 (1993).
39. Halsey, T. C. Electrodeposition and diffusion-limited aggregation. *J. Chem. Phys.* 92, 3756–3767 (1990).
40. Garik, P. *et al.* Laplace-field-controlled and diffusion-field-controlled growth in electrochemical deposition. *Phys. Rev. Lett.* 62, 2703–2706 (1989).
41. Argoul, F., Arneodo, A., Grasseau, G. & Sornay, H. L. Self-similarity of diffusion-limited aggregates and electrodeposition clusters. *Phys. Rev. Lett.* 61, 2558–2561 (1988).
42. Savada, V., Dougherty, A. & Gollub, J. P. Dendritic and fractal patterns in electrolytic metal deposits. *Phys. Rev. Lett.* 56, 1260–1263 (1986).
43. Keh, H. J. & Li, W. J. Interactions among bipolar spheres in an electrolytic cell. *J. Electrochem. Soc.* 141, 3103–3114 (1994).

**Acknowledgments.** We thank J. Yuan, M. Vallieres and A. Nath for discussions. This work was supported by Drexel University.

Correspondence and requests for materials should be addressed to J.-C.B. (e-mail: brailej@post.drexel.edu).

## The interplay between binding energy and catalysis in the evolution of a catalytic antibody

Helle D. Ulrich<sup>††</sup>, Emily Mundorff<sup>†</sup>,  
Bernard D. Santarsiero<sup>†</sup>, Edward M. Driggers<sup>††</sup>,  
Raymond C. Stevens<sup>†</sup> & Peter G. Schultz<sup>††</sup>

<sup>†</sup> Howard Hughes Medical Institute, and <sup>††</sup> Materials Science Division, Lawrence Berkeley National Laboratory and Department of Chemistry, University of California, Berkeley, Berkeley, California 94720, USA

Antibody catalysis<sup>1</sup> provides an opportunity to examine the evolution of binding energy and its relation to catalytic function in a system that has many parallels with natural enzymes. Here we report such a study involving an antibody AZ-28 that catalyses an oxy-Cope rearrangement, a pericyclic reaction that belongs to a well studied and widely used class of reactions in organic chemistry<sup>2</sup>. Immunization with transition state analogue 1 results in a germline-encoded antibody that catalyses the rearrangement of hexadiene 2 to aldehyde 3 with a rate approaching that of a related pericyclic reaction catalysed by the enzyme chorismate mutase<sup>3</sup>. Affinity maturation gives antibody AZ-28, which has six amino acid substitutions, one of which results in a decrease in catalytic rate. To understand the relationship between binding and catalytic rate in this system we characterized a series of active-site mutants and determined the three-dimensional crystal structure of the complex of AZ-28 with the transition state analogue. This analysis indicates that the activation energy depends on a complex balance of several stereoelectronic effects which are controlled by an extensive network of binding interactions in the active site. Thus in this instance the combinatorial diversity of the immune system provided both an efficient catalyst for a reaction where no enzyme is known, as well as an opportunity to explore the mechanisms and evolution of biological catalysis.

Monoclonal antibody AZ-28 catalyses the unimolecular oxy-Cope rearrangement of substrate 2 to product 3 (which is trapped *in situ* as the oxime) with a rate acceleration ( $k_{cat}/k_{uncat}$ ) of 5,300 (Fig. 1a)<sup>4</sup>. To determine the origins of the binding and catalytic properties of this antibody, its immunological precursor was cloned in the form of the germline variable-region (V<sub>L</sub> and V<sub>H</sub>, where L and H represent light and heavy chains, respectively) genes<sup>5,6</sup> (Fig. 1b). During affinity maturation, the precursor to AZ-28 V<sub>L</sub>, the T1/B V<sub>L</sub> germline segment<sup>7</sup>, underwent five silent mutations as well as two amino-acid replacements: at position 34 on the light chain, serine was substituted by asparagine (Ser<sup>L34</sup> to Asn) in complementarity-

determining region CDR1 and Ala<sup>L51</sup> to Thr in CDR2. The precursor to AZ-28 V<sub>H</sub>, the VH 19.1.2 germline segment<sup>8</sup>, underwent four somatic mutations, Tyr<sup>H32</sup> to Phe in CDR1, Ser<sup>H56</sup> to Gly and Asn<sup>H58</sup> to His in CDR2, and Thr<sup>H73</sup> to Lys in framework region FR3, without any silent changes. CDR3 could be derived from the diversity (D) regions D<sub>SP2.2</sub> (Asp<sup>H100</sup>) or D<sub>SP2.3</sub>, D<sub>SP2.4</sub>, or D<sub>SP2.6</sub> (Gly<sup>H100</sup>)<sup>9</sup>, alternatively, as AZ-28 was generated from an outbred mouse strain, it might be derived from an unmutated (wild-type) non-standard D region. Considering that a two-nucleotide change would be necessary to convert Gly or Asp to Phe<sup>H100</sup>, this latter possibility seems more likely.

To determine the effects of affinity maturation on binding and catalysis, we reconstructed the pure germline (no somatic mutations) version of AZ-28. In addition, all six somatic mutations were reintroduced into the germline antibody individually as well as in combinations that varied according to their chains. Binding affinities and kinetics for hapten 1 were measured by surface plasmon resonance (Table 1). The heavy and light chains provide nine- and fivefold improvements in affinity, respectively, indicating that the effects of both chains are largely additive<sup>10</sup>. The resulting 40-fold overall decrease in the dissociation constant  $K_d$  (1) from 670 to 17 nM is well within the range reported for other antibodies to small haptens from secondary immune responses<sup>11</sup>. Transition-state theory dictates that rate enhancement should correlate with increased differential binding of the antibody for the transition state relative to substrate<sup>12,13</sup>. Surprisingly, however, the germline form of AZ-28, which has approximately the same Michaelis constant ( $K_M$ ) and hence affinity for substrate as does mature AZ-28, affords a 35-fold greater rate enhancement compared with mature AZ-28 (the chemical step is rate-limiting in the case of the mature antibody)<sup>14</sup>. Moreover, mutation of Phe<sup>H100</sup> to Asp in the germline antibody leads to an even greater rate acceleration ( $k_{cat}/k_{uncat} = 3 \times 10^5$ ), despite a lower affinity for hapten 1. This improvement in catalytic efficiency results in a rate enhancement approaching that of the well characterized enzyme chorismate mutase, which catalyses a related [3,3] sigmatropic rearrangement<sup>1</sup>.

Analysis of the germline single mutants indicates that whereas five of the six somatic mutations significantly affect binding affinity, the enhanced catalytic efficiency of the germline antibody compared to AZ-28 is associated largely with the mutation of Ser<sup>L34</sup> to Asn. Kinetic data from the hybrid antibody L<sup>34</sup>H<sup>100</sup> (in which the light chain of the germline antibody is paired with the heavy chain of AZ-28) and the germline Ala<sup>L51</sup>Thr mutant (Table 1) together indicate that the change of Asn<sup>L34</sup> to Ser in the affinity matured antibody, AZ-28, leads to a 20-fold increase in  $k_{cat}$ . We further examined this dominant role of position L34 by site-directed mutagenesis. Substitution of Ala or Asp for Ser<sup>L34</sup> in the germline antibody resulted in rate enhancements intermediate between that of the germline and mature antibody (Table 1), whereas substitution of His and Glu at this position led to decreases in activity of more than 250- and 2,500-fold, respectively. Measurement of the pH dependence of hapten dissociation rates in the range of pH 4.0 to 7.4 indicated that the only titratable group with an influence on hapten binding was Asp<sup>L34</sup>, with the protonated form approaching the behaviour of Asn in this position. In contrast, the binding of the germline antibody and the germline mutants Ser<sup>L34</sup> to Asn and Phe<sup>H100</sup> to Asp, was essentially independent of pH<sup>15</sup>.

To understand the relationship better between the binding and catalytic activities of this series of related antibodies, we determined the three-dimensional crystal structure of the AZ-28 antigen-binding fragment (Fab) complexed with hapten 1 at 2.6 Å resolution. The hapten is bound in a deep, cylindrical cavity, about 8.3 Å wide and 18.5 Å deep; approximately 85% of hapten 1 (excluding linker) is buried within the Fab (Figs 2–4). Hapten 1 is bound in a chair-like geometry with the aryl and hydroxyl substituents of the cyclohexyl ring equatorial. The phenyl substituents of hapten 1 are rotated with respect to each other by a dihedral angle of 19° and make extensive

contacts with the active site residues. The 5-phenyl group of hapten 1 is buried at the bottom of the cavity and surrounded by the side chains of Trp<sup>H47</sup>, Trp<sup>H103</sup>, Phe<sup>L36</sup>, Leu<sup>L89</sup>, Phe<sup>L98</sup>, Ala<sup>H93</sup> and Glu<sup>H35</sup> (Fig. 3). The 2-phenyl substituent is located near the opening of the binding pocket and its orientation is fixed by a  $\pi$ -stacking interaction with the imidazole ring of His<sup>H96</sup> and van der Waals interactions with the side chain of Tyr<sup>L91</sup>. The cyclohexyl ring of hapten 1, which mimics the cyclic 4 $\pi$  + 2 $\sigma$  transition state, is rotated out of the planes of the 5- and 2-phenyl rings by 81° and 85°, respectively (Fig. 3). Its position is fixed by hydrogen-bonding interactions between the hydroxyl substituent of hapten 1 and both the imidazole ring and backbone amide NH group of His<sup>H96</sup>. There is also a water molecule bridging the hydroxyl substituent with the

carboxylate group of Glu<sup>H50</sup>. The cyclohexyl ring of hapten 1 is also in van der Waals contact with the hydrophobic side chains of Tyr<sup>L91</sup>, Tyr<sup>L96</sup> and Tyr<sup>H100a</sup> and the hydrophilic side chains of Asn<sup>L34</sup> and Asp<sup>H101</sup>. The linker arm is exposed to solvent and adopts multiple conformations in the crystal structure.

The X-ray crystal structure suggests that antibody AZ-28 functions by a combination of entropic<sup>16</sup> and electronic effects. The antibody binds hapten 1 in a chair-like conformation, consistent with the preferred chair transition state of the Cope rearrangement<sup>17</sup>. The positions of the C2 and C5 atoms of hapten 1, and as a consequence, the C2 and C5 atoms of hexadiene 2, are fixed by extensive van der Waals interactions by the two phenyl substituents. Consequently, the bound conformation of the acyclic

Table 1 Binding and catalytic properties of AZ-28 and related antibodies

Antibody	$k_{cat}$ (min <sup>-1</sup> )	$K_M$ ( $\mu$ M)	$k_{cat}/K_{uncat}$	$k_{on}$ (10 <sup>5</sup> M <sup>-1</sup> s <sup>-1</sup> )	$k_{off}$ (10 <sup>-2</sup> s <sup>-1</sup> )	$K_D$ (10 <sup>-6</sup> M)	$\Delta\Delta G$ (kcal mol <sup>-1</sup> )
AZ-28	0.023 (0.002)	74 (12)	$5 \times 10^3$	3.11 (0.46)	0.55 (0.02)	17	-2.2
L <sup>H47</sup>	0.46 (0.03)	143 (14)	$94 \times 10^3$	1.49 (0.08)	1.37 (0.02)	82	-1.2
H <sup>L103</sup>	0.076 (0.006)	206 (31)	$16 \times 10^3$	0.47 (0.02)	0.64 (0.01)	152	-0.9
G	0.80 (0.06)	73 (13)	$163 \times 10^3$	0.30 (0.01)	1.90 (0.08)	670	0.0
G(S <sup>L34</sup> N)	0.076 (0.005)	78 (17)	$16 \times 10^3$	0.49 (0.03)	0.70 (0.01)	150	-0.9
G(A <sup>L91</sup> T)	0.83 (0.08)	19 (3)	$169 \times 10^3$	0.31 (0.01)	1.59 (0.03)	686	0.0
G(S <sup>L34</sup> A)	0.18 (0.01)	108 (10)	$45 \times 10^3$	0.30 (0.02)	2.42 (0.04)	815	0.1
G(S <sup>L34</sup> D)	0.22 (0.01)	59 (5)	$135 \times 10^3$	0.19 (0.05)	2.96 (0.02)	1282	0.4
G(Y <sup>H42</sup> F)	0.68 (0.02)	78 (8)	$153 \times 10^3$	1.04 (0.17)	1.62 (0.00)	162	-0.8
G(S <sup>L56</sup> G)	0.75 (0.03)	90 (12)	$145 \times 10^3$	0.77 (0.06)	1.79 (0.01)	206	-0.7
G(N <sup>H38</sup> H)	0.71 (0.04)	75 (8)	$165 \times 10^3$	0.50 (0.04)	1.21 (0.01)	211	-0.7
G(T <sup>H173</sup> K)	0.81 (0.04)	123 (9)	$296 \times 10^3$	0.55 (0.05)	1.62 (0.02)	309	-0.5
G(F <sup>H100</sup> D)	1.45 (0.05)	19 (1)	$92 \times 10^3$	0.39 (0.08)	2.75 (0.02)	840	0.1
G(F <sup>H100</sup> G)	0.45 (0.01)			0.45 (0.03)	2.42 (0.01)	512	-0.2

G, full germline clone; L<sup>H47</sup>, combination of germline V<sub>H</sub> with mature V<sub>H</sub>; H<sup>L103</sup>, combination of germline V<sub>H</sub> with mature V<sub>L</sub>; single point mutations are indicated in the single-letter amino-acid code in parentheses. Standard deviations are given in parentheses.  $\Delta\Delta G$  is the difference in free energy, calculated relative to the germ line.

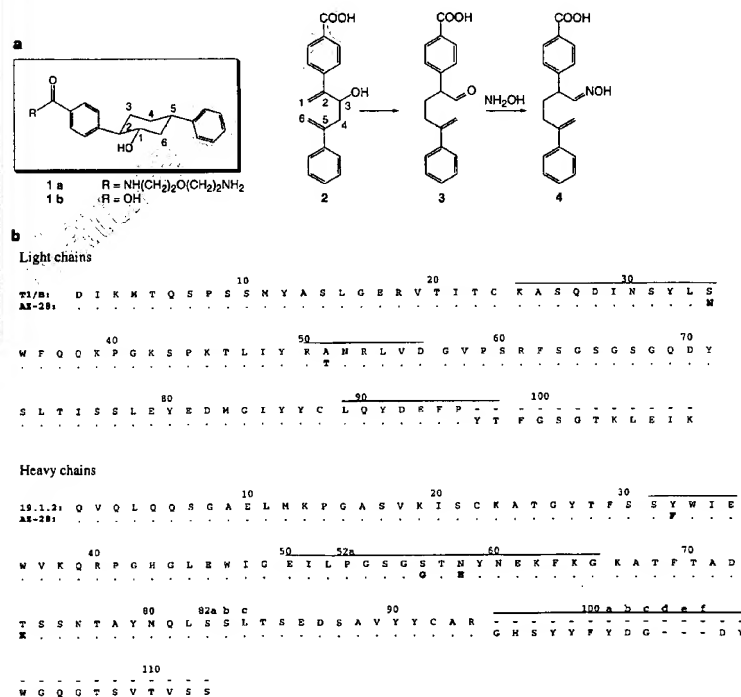


Figure 1 a, Transition-state analogue (hapten 1, a and b derivatives) and the oxy-Cope rearrangement reaction catalysed by antibody AZ-28. b, Light- and heavy-chain variable region sequences of AZ-28, and the germline precursors V1-T1/B and V1-19.1.2. Amino acids are represented in the one-letter code. Numbering is according to ref. 26. CDRs, complementarity determining regions, are indicated by bars.

( $4\pi + 2\sigma$ ) system of hexadiene 2 should be close to that of the transition state of either a stepwise or concerted rearrangement reaction<sup>18,19</sup>. This is consistent with NMR studies that show transfer nuclear Overhauser effects (NOEs) between the terminal olefinic protons of substrate 2 when bound in the antibody active site<sup>14</sup>.

In addition to proper orbital alignment of the ( $4\pi + 2\sigma$ ) orbitals, electronic effects arising from the 2,5-diphenyl and 3-hydroxyl substituents affect the energetics of 3,3-sigmatropic rearrangement reactions. Hyperconjugation of electron density on oxygen accelerates the oxy-Cope rearrangement through an anionic substituent effect<sup>20</sup>. Consequently, His<sup>H56</sup> and Glu<sup>H50</sup> might act to enhance the rate of the rearrangement by increasing the electron density on the oxygen substituent of substrate 2. The orientation of the latter residue may be affected by the somatic mutation of Asn<sup>H58</sup> to His and Ser<sup>H56</sup> to Gly. In addition to effects associated with the hydroxyl substituent, aryl substituents at the 2 and 5 positions of 1,5-hexadiene have also been shown to lower the activation energy by 5 to 10 kcal mol<sup>-1</sup> (this effect has been attributed to stabilization of a biradicaloid-like transition state<sup>21</sup>). Hydrogen-bonding interactions with the hydroxyl group, however, probably rotate the two  $\pi$  bonds of the 1,5-hexadiene out of planarity with the two phenyl substituents, leading to decreased  $\pi$ -orbital overlap and an increase in

activation energy (Fig. 3). Thus the rate of the antibody AZ-28-catalysed reaction depends on a balance of the stereoelectronic effects involving alignment of the ( $4\pi + 2\sigma$ ) orbitals of the diene, the degree of electron density on the hydroxyl substituent and the  $\pi$ -orbital overlap with the aryl substituents.

The crystal structure also provides an explanation for the inverse correlation of binding affinity to hapten 1 and catalytic rate. During the process of affinity maturation, increased binding interactions between antibody and hapten fix the orientation of the phenyl substituents with respect to the cyclohexyl ring. Consequently, upon substrate binding to mature AZ-28, the hexadiene core probably rotates with respect to the phenyl substituents to increase hydrogen-bonding and packing interactions (Fig. 3), making it more difficult to achieve maximal orbital overlap than in the case of the germline antibody, where the hapten is bound less tightly. Asn<sup>L34</sup> is 3.8 Å from the cyclohexyl ring and directly interacts with Tyr<sup>H100a</sup> and Asp<sup>H101</sup> of V<sub>H</sub>CDR3 to help fix the conformation of the bound hapten. Thus this residue might be expected to have the largest effect on the shape of the active site, and as a consequence on the stereoelectronic features of the reaction coordinate. Consistent with this model, variation in the structure of V<sub>H</sub> CDR3, which is important for orienting the 2-phenyl substituent, also leads to large variations in

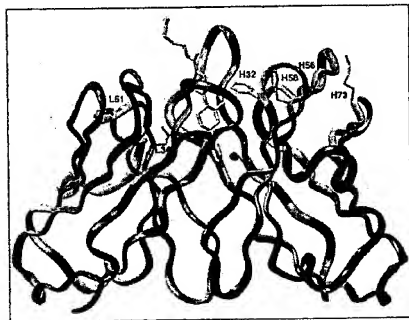


**Figure 2** The three-dimensional structure of the variable domain of the AZ-28 Fab-hapten 1 complex showing the bound transition-state analogue (yellow) and sites of somatic mutation: Asn<sup>L34</sup>, Thr<sup>L51</sup>, Phe<sup>L32</sup>, Gly<sup>H56</sup>, His<sup>H58</sup> and Lys<sup>H73</sup> (green); the alpha-carbon (Ca) backbone of V<sub>H</sub> and V<sub>L</sub> are in blue and red, respectively (heteroatom colours: O, red; N, blue).

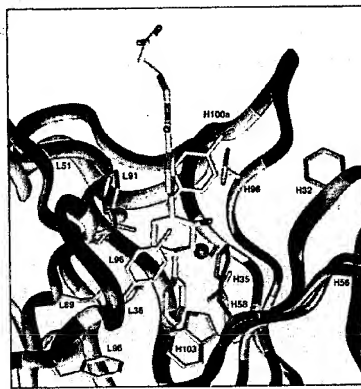


**Figure 3** Structure of the AZ-28 active site showing the transition-state analogue 1 in yellow. The 5-phenyl ring is buried in the hydrophobic pocket and the 2-phenyl ring and linker are near the surface; the Ca backbone of V<sub>H</sub> and V<sub>L</sub> are in blue and red, respectively, and sites of somatic mutation are indicated in green. The side chains of active-site residues interacting with hapten are indicated in brown. Two water molecules in the active site are indicated as red spheres (heteroatom colours: O, red; N, blue).

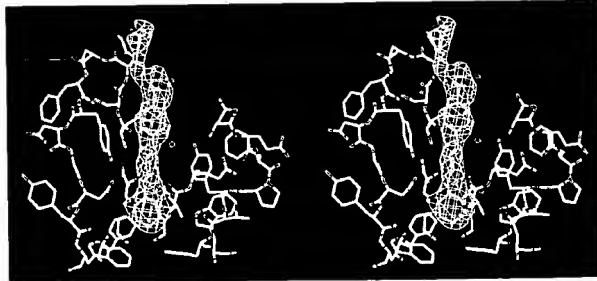


**Figure 4** Stereodiagram of a 1F5-F5 electron density map, illustrating the electron density in the antibody combining site. The electron density map was contoured at 2.2σ.

catalytic activity among a series of related antibodies, with Vh of AZ-28 being the most effective<sup>22</sup>.

Functional and structural analysis of the binding and catalytic properties of AZ-28 and related antibodies indicates that an extended network of hydrogen-bonding and hydrophobic interactions act together to control the stereoelectronic features of this reaction. Affinity based selection in response to hapten 1 leads to favourable orbital alignment of the ( $4\pi + 2\sigma$ ) system of the diene and favourable interactions with the hydroxyl substituent. However, introduction of the somatic mutation Ser<sup>134</sup> to Asn, which leads to a modest increase in binding affinity, affects the relative orientation of the diene and phenyl orbitals, and therefore results in a significant decrease in rate<sup>23</sup>. This inverse correlation of rate enhancement and affinity stems from the fact that rotation of the aryl substituents is not restricted in hapten 1, as it is in the lowest-energy transition state. Nonetheless, the combinatorial diversity of the immune system, when selected by using mechanistic information programmed into hapten 1, afforded an efficient antibody catalyst for an oxy-Cope rearrangement, a reaction for which there is no known enzyme. Improvements in hapten structure, together with mutations that optimize orbital alignment, should further increase catalytic efficiency<sup>24,25</sup>. Finally, our study illustrates how catalytic antibodies can help us to understand the complex relationship between binding energy and catalysis in the evolution of biological catalysts. □

# Methods

**Cloning of germline antibody and construction of mutants.** T1/B- was identified as a potential germline candidate through a homology search of the Kabat database<sup>26</sup>. Based on its published 5' flanking region<sup>27</sup>, a primer for the polymerase chain reaction (PCR) was designed to amplify the Vh-coding region and upstream flanking DNA from both AZ-28 hybridoma DNA and unrearranged murine liver DNA (of Swiss Webster origin). A primer based on the 3' untranslated region served for the amplification of unrearranged DNA, whereas primer J<sub>h</sub>4 (ref. 5) was used for hybridoma DNA. Several clones of both PCR products were sequenced and their flanking regions were found to be identical with the published T1/B- sequence. The PCR primer for analogous amplification of the Vh genes was designed based on the published 5' untranslated region of 37A11 Vh<sup>28</sup> (ref. 27), a mutated version of 19.1.2 Vh (ref. 8). This primer, in combination with oligonucleotides covering the AZ-28 D region and the 3' end of the 19.1.2 Vh region, was used to amplify Vh and 319 nucleotides of 5' flanking region from AZ-28 hybridoma DNA and liver DNA, respectively. Two distinct 5' untranslated sequences were obtained from several clones of PCR product from liver DNA, one of which was identical to the corresponding region from AZ-28 hybridoma DNA. Its coding region—identical to that of 19.1.2—was therefore concluded to be the authentic AZ-28 germline sequence. The following modifications were made to the previously described expression system<sup>27</sup>: the M13 origin of pUC118 was inserted as blunt *Apal*/*NarI* fragment into the *MscI* site of p4xH (ref. 5), yielding p4xH-M13. The V regions from pAZ-28 (ref. 6) were fitted by PCR with their authentic N termini, as determined from their germline sequences, and subcloned into p4xH-M13, resulting in pAZ-28\*. The germline Vh region was inserted in the same way, whereas the germline Vh region and all single mutants were constructed by site-directed mutagenesis, using sense oligonucleotides and avoiding rare codons.

**Crystallization and structure determination.** Antibody AZ-28 was crystallized in 25% PEG 1000, 0.1 M sodium acetate, pH 4.6, 0.3 M CdCl<sub>2</sub> and 0.1 M (NH<sub>4</sub>)<sub>2</sub>SO<sub>4</sub> in the presence of 2 mM hapten 1, using the hanging-drop method. The crystals grew as very thin plates (0.4 mm × 0.3 mm × 0.02 mm). Data were collected at Stanford Synchrotron Radiation laboratory beamline 7-1 and processed using DENZO and SCALEPACK<sup>29</sup>. The space group was P<sub>2</sub>, with two molecules in the asymmetric unit, and unit cell parameters were:  $a = 42.78 \text{ \AA}$ ,  $b = 81.50 \text{ \AA}$ ,  $c = 128.2 \text{ \AA}$ ,  $\beta = 93.43^\circ$ . The structure was solved using molecular replacement. The AMoRe<sup>30</sup> package was used to search a library of variable domains using data between 8.0 and 3.5 Å. A solution for the variable domain was found with the model from 6FAB<sup>30</sup>, with a correlation coefficient of 28.8% (R factor, 48.4%). Fixing this solution brought out the

second variable domain with a correlation coefficient of 28.6% (R factor, 48.9%). Mutation of the molecular replacement model and rebuilding was done using program O (ref. 31). Refinement was carried out using positional, simulated annealing and torsional refinement in X-PLOR, with NCS restraints turned on<sup>32</sup>. A total of 24,768 reflections were used in the refinement between 20.0–2.6 Å. Maps were produced using the CCP4 (ref. 33) package and interpreted in O. The electron density of the hapten was clearly observed in a  $1F_o - F_c$  map. The data were 91.1% complete to 2.6 Å resolution with an R-merge of 6.0%. A total of 193 water molecules were placed in the structure. The final model has a free R of 30.0% and crystallographic R of 20.0%.

**Characterization of the binding and catalytic properties of AZ-28 and related antibodies.** All antibodies were expressed and purified as recombinant Fab fragments in *Escherichia coli* as described<sup>34</sup>. For surface plasmon resonance measurements, Fab fragments were additionally passed through a Superdex-75 column. Protein concentrations were determined spectrophotometrically based on calculated extinction coefficients at 280 nm. Structural integrity of the proteins was confirmed by circular dichroism. Catalytic constants were measured at 5 or 6 substrate concentrations in an HPLC assay<sup>3</sup> in 20 mM MES, pH 6.0, 150 mM NaCl, 5 mM hydroxylamine, 4% acetonitrile, and 1% DMSO, with enantiomerically pure substrate<sup>3</sup> and 30  $\mu\text{M}$  o-nitroanisole as internal standard. AZ-28 and H<sub>2</sub>L<sup>24</sup> were used at 1.0  $\mu\text{M}$ , all other clones at 0.1  $\mu\text{M}$ . Rates were fitted to the Michaelis-Menten equation using the program Kaleidagraph. Affinity measurements were carried out in 20 mM MES, pH 6.0, 150 mM NaCl, and 0.005% P20 (Pharmacia) by surface plasmon resonance using a Biacore 2000 biosensor (Pharmacia). Sensor chips (CM5, research grade) were derivatized with the BSA-conjugate of hapten 1a at 530–700 resonance units (RU) using the amine-coupling method.  $K_d$  values were determined under equilibrium conditions (20–30 min injections at 3  $\mu\text{l min}^{-1}$ , subtracting the signal obtained from a surface derivatized with unconjugated BSA) at 5 or 6 concentrations encompassing the  $K_d$ . Association rates were determined at 4 or 5 concentrations above the  $K_d$  at a flow rate of 20  $\mu\text{l min}^{-1}$ . The values of  $k_{\text{on}}$  were calculated from nonlinear curve fittings using the simple association model of the supplied software (Pharmacia Biosensor) and averaged. Fittings were started 10 s after the start of injection, covering 30–200 s of the association phase and avoiding phases of chip saturation. Residuals were in the range of <1 to a few RU. Dissociation rates were measured using saturation concentrations of Fab and a flow rate of 20  $\mu\text{l min}^{-1}$ . Fittings were from 10 to 40 s after the start of the dissociation phase. Increases in flow rate or inclusion of 400  $\mu\text{M}$  free hapten 1 had no further effect on the calculated  $k_{\text{off}}$  values (results not shown).

Received 15 April; accepted 21 July 1997.

- Schultz, P. G. & Lerner, R. A. From molecular diversity to catalysis: lessons from the immune system. *Science* **269**, 1835–1842 (1995).
- Woodward, R. B. & Hoffmann, R. *The Conservation of Orbital Symmetry* (Academic, New York, 1970).
- Andrews, P. R., Smith, G. D. & Young, I. G. Transition-state stabilization and enzymic catalysis. Kinetic and molecular orbital studies of the rearrangement of chorismate to prephenate. *Biochemistry* **12**, 3492–3498 (1973).
- Braisted, A. C. & Schultz, P. G. An antibody-catalyzed oxy-Cope rearrangement. *J. Am. Chem. Soc.* **116**, 2211–2212 (1994).
- Ulrich, H. D., Patten, P. A., Yang, P. L., Romberg, F. E. & Schultz, P. G. Expression studies of catalytic antibodies. *Proc. Natl Acad. Sci. USA* **92**, 11907–11911 (1995).
- Ulrich, H. D., Driggers, E. M. & Schultz, P. G. Antibody catalysis of pericyclic reactions. *Acta Chem. Scand.* **50**, 328–332 (1996).
- Pech, M., Höchli, J., Schell, H. & Zachau, H. G. Differences between germ-line and rearranged immunoglobulin Vh coding sequences suggest a localized mutation mechanism. *Nature* **291**, 668–670 (1981).
- Abulafia, P. N. et al. Different Vh and Vh germline genes are used to produce similar combining sites with specificity for (4E – 4E) dextran. *J. Immunol.* **138**, 4472–4477 (1987).
- Kurawawa, Y. & Tonegawa, S. Organization, structure, and assembly of immunoglobulin heavy chain diversity DNA segments. *J. Exp. Med.* **155**, 201–218 (1982).
- Patten, P. A. et al. The immunological evolution of catalysis. *Science* **271**, 1086–1091 (1996).
- Berek, C., Griffiths, G. M. & Milstein, C. Molecular events during maturation of the immune response to oxazolone. *Nature* **316**, 412–418 (1985).
- Haldane, J. B. S. *Enzymes* (Longmans, Green & Co, London, 1930).
- Pauling, L. *Chem. Eng. News* **24**, 1375 (1946).
- Driggers, E. M. et al. Mechanistic studies of an antibody-catalyzed oxy-Cope rearrangement. *J. Am. Chem. Soc.* (submitted).
- Ulrich, H. Recombinant catalytic antibodies. thesis, Univ. California, Berkeley, 1996.
- Page, M. I. & Jencks, W. P. Entropic contributions to rate accelerations in enzymic intramolecular reactions and the chelate effect. *Proc. Natl Acad. Sci. USA* **68**, 1678–1683 (1971).
- Doering, W. E. & Roth, W. R. The overlap of two allyl radicals or a four-centered transition state in the Cope rearrangement. *Tetrahedron* **18**, 67–74 (1962).
- Gajewski, J. J. Energy surfaces of sigmatropic shifts. *Acc. Chem. Res.* **13**, 142–148 (1980).
- Gajewski, J. J. & Gee, K. R. Solvent, counterion, and secondary deuterium kinetic isotope effects in the anionic oxy-Cope rearrangement. *J. Am. Chem. Soc.* **113**, 967–971 (1991).
- Seigrist, M. J., Goddard, W. A. & Evans, D. A. Theoretical studies of the oxy-anionic substituent effect. *J. Am. Chem. Soc.* **101**, 1994–1997 (1979).

21. Dewar, M. J. S. & Wade, L. E. A study of the mechanism of the cope rearrangement. *J. Am. Chem. Soc.* **99**, 4417–4424 (1977).
22. Ulrich, H. D. & Schultz, P. G. The evolution of binding affinity and catalysis in a family of catalytic antibodies. *J. Mol. Biol.* (submitted).
23. Storm, D. R. & Koshland, D. E. Jr. A source for the special catalytic power of enzymes: Orbital steering. *Proc. Natl Acad. Sci. USA* **66**, 445–452 (1970).
24. Janda, K. D. et al. Direct selection for a catalytic mechanism from combinatorial antibody libraries. *Proc. Natl Acad. Sci. USA* **91**, 2532–2536 (1994).
25. Tawfik, D. S., Green, B. S., Chap, R., Sela, M. & Eshkol, Z. catELISA: A facile general route to catalytic antibodies. *Proc. Natl Acad. Sci. USA* **98**, 373–377 (1993).
26. Kabat, E. A., Wu, T. T., Perry, H. M., Gottesman, K. S. & Foeller, C. *Sequences of Proteins of Immunological Interest* (US Dept of Health and Human Services, National Institutes of Health, Bethesda, 1991).
27. Nahmias, C., Strosberg, A. D. & Emonet, L. J. The immune response toward  $\beta$ -adrenergic ligands their receptors. VIII. Extensive diversity of V $\alpha$  and V $\beta$  genes encoding anti-alprenolol antibodies. *J. Immunol.* **140**, 1304–1311 (1988).
28. Otwinowski, Z. & Minor, W. Processing of X-ray diffraction data collected in oscillation mode. *Meth. Enzymol.* **276**, 307–325 (1996).
29. Navaza, J. AMOR: An automated package for molecular replacement. *Acta Crystallogr. A* **50**, 157–163 (1994).
30. Strong, R. K. et al. Three-dimensional structure of a murine anti-P-azophenylarsenate FAB 36-71. I. X-ray crystallography, site-directed mutagenesis, and modeling of the complex with hapten. *Biochemistry* **30**, 3739–3748 (1991).
31. Jones, T. A., Zou, J.-Y., Cowan, S. W. & Kjeldgaard, M. Improved methods for building protein models in electron density maps and the location of errors in these models. *Acta Crystallogr. A* **47**, 110–119 (1991).
32. Brünger, A. X-PLOR, Version 3.851. *A System for X-ray Crystallography and NMR* (Yale Univ. Press, New Haven, Connecticut, 1996).
33. Collaborative Computational Project Number 4. The CCP4 suite: Programs for protein crystallography. *Acta Crystallogr. D* **50**, 760–763 (1994).

**Acknowledgements.** We thank M. Conn for precursor to the hapten, C. Che and P. Yang for helpful discussions, and the Stanford Synchrotron Radiation Laboratory for synchrotron beam time. We are grateful for financial support for this work from the US Department of Energy and the NIH. P.G.S. is a HHMI investigator; H.D.U. was supported by a predoctoral fellowship from the NSF.

Correspondence and requests for materials should be addressed to R.C.S. or P.G.S.

## Sources and contribution of terrigenous organic carbon to surface sediments in the Gulf of Mexico

Miguel A. Goñi\*, Kathleen C. Ruttenberg† & Timothy I. Eglinton†

\* Department of Geological Sciences, University of South Carolina, Columbia, South Carolina 29208, USA

† Department of Marine Chemistry and Geochemistry, Woods Hole Oceanographic Institution, Woods Hole, Massachusetts 02543, USA

The sources and burial processes of organic matter in marine sediments are not well understood, yet they are important if we are to have a better understanding of the global carbon cycle<sup>1</sup>. In particular, the nature and fraction of the terrestrial organic carbon preserved in marine sediments is poorly constrained. Here we use the chemical and stable carbon isotope signatures of oxidation products from a macromolecular component (lignin)<sup>2</sup> of the terrigenous organic matter preserved in offshore surface sediments in the Gulf of Mexico to complement similar data from an existing onshore transect<sup>3</sup> in this region. The complete onshore-offshore data set, along with radiocarbon dates of the bulk organic material at the same sites, allows the differentiation of material originating from plants that photosynthesize using the  $C_4$  mechanism from those that undergo  $C_3$  photosynthesis. We conclude that the offshore lignins derive from erosion of the extensive grassland ( $C_4$ ) soils of the Mississippi River drainage basin, and that the nearshore lignins originate largely from  $C_3$  plant detritus from coastal forests and swamps. This distribution is probably due to the hydrodynamic sorting of the different source materials<sup>4</sup> during their seaward transport. These results suggest that previous studies<sup>3,5</sup> have significantly underestimated the terrigenous fraction of organic matter in offshore sediments by not recognizing the contribution of  $C_4$  vegetation to the carbon-isotope composition. Such an under-

estimate may force revisions in the assessment of past marine primary productivity and associated organic carbon fluxes<sup>6</sup>, and of organic matter preservation/remineralization<sup>7</sup> and nutrient cycling<sup>8</sup> in marine sediments.

The Gulf of Mexico is an extensively studied marine environment in which the fraction of organic carbon preserved in marine sediments that is of terrigenous origin ( $OC_{terr}$ ) may be particularly high, owing to the proximity of continental land masses. Draining an area<sup>9</sup> of  $3.3 \times 10^6$  km<sup>2</sup>, which includes most of North America's grasslands<sup>10</sup> (Fig. 1), the Mississippi River system is the predominant source of sediment<sup>7</sup> and fresh water<sup>11</sup> to the Gulf. We collected surface (0–2 cm) sediments from two transects perpendicular to the shore extending across the shelf and slope (Fig. 1). The elemental and isotopic compositions of organic matter from these sediments are shown in Table 1.

Conventional  $^{14}C$  ages of bulk sedimentary OC range between 2,580 and 6,770 yr BP and generally increase with water depth. On the basis of published sedimentation rates<sup>12</sup>, the average ages of marine phytodetritus in surface (0–2 cm) sediments should range between 3 (nearshore) and 400 (offshore) calendar yr. The large difference between  $^{14}C$  and estimated calendar ages suggests that, even after accounting for sediment mixing and the reservoir effect on marine OC (ref. 13), a significant fraction of the sedimentary OC must be relatively 'old', and most likely allochthonous in origin. Moreover, because  $OC_{terr}$   $^{14}C$  ages are not subject to oceanic reservoir corrections, this material must be composed to a large extent of reworked OC (ref. 14). Non-zero apparent  $^{14}C$  ages for surface sediments are commonly observed on continental shelf or

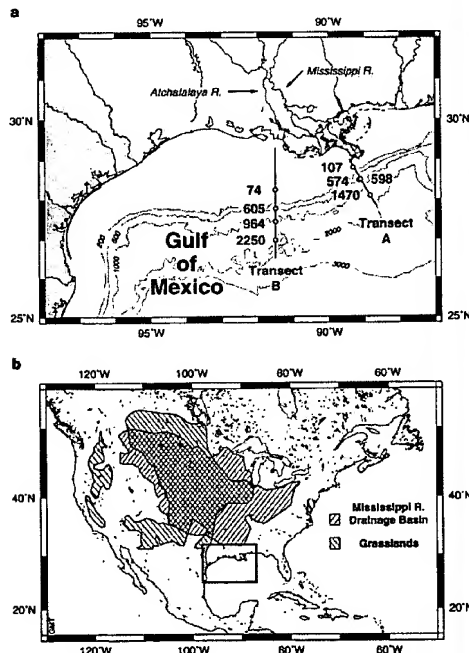


**Figure 1** a, Map of the sampling locations and water depths (m) in the Gulf of Mexico. b, Map of the extent of the drainage basin of the Mississippi River and the grasslands in North America<sup>10</sup>. The area shown in a is an enlargement of the box in b.